Long-range transport of Asian dust to the Arctic: identification of transport pathways, evolution of aerosol optical properties, and impact assessment on surface albedo changes

Xiaoxi Zhao[1], Kan Huang[1,3,4*], Joshua S. Fu[2], Sabur F. Abdullaev[5]

[1]Center for Atmospheric Chemistry Study, Shanghai Key Laboratory of Atmospheric Particle Pollution and Prevention (LAP[3]), Department of Environmental Science and Engineering, Fudan University, Shanghai, 200433, China

[2]Department of Civil and Environmental Engineering, University of Tennessee, Knoxville, TN, USA

[3]IRDR ICoE on Risk Interconnectivity and Governance on Weather/Climate Extremes Impact and Public Health, Fudan University, Shanghai 200433, China

[4]Institute of Eco-Chongming (IEC), Shanghai, 202162, China

[5]Physical Technical Institute of the Academy of Sciences of Tajikistan, Dushanbe, Tajikistan

Corresponding author: huangkan@fudan.edu.cn

Abstract

Airborne dust is one of the most important natural aerosols, it has various environmental impacts on air quality, ocean fertilization, and the global climate change. Asian dust, representing one of the major dust sources in the world, has been widely studied due to its long-range transport capability. However, its transport to the Arctic has been less investigated. In this study, two typical transport routes were identified based on the recorded dust events in China during 2011-2015. Accordingly, two specific

Asian dust long-range transport events were selected and compared, i.e., one observed at Barrow, Alaska (travelled mostly over lands within 6-7 days) and the other one observed at Alert, Canada (travelled mostly over oceans within 7-8 days). The transport routes of the two dust events had been cross-validated by using air mass trajectory modeling, meteorology reanalysis data, ground-based aerosol columnar and profiling observations, and spaceborne remote sensing. It was found that different transport routes to the Arctic had divergent effects on the evolution of aerosol properties, revealing different mixing extents between dust, anthropogenic particles, smoke, and sea salts. Based on the SNow ICe Aerosol Radiative model, the albedo simulation indicated that dust and elemental carbon together reduced the surface albedo by 0.35% to 2.63% compared to the pure snow condition. This study implied that the dust long-transport from China to the Arctic was ubiquitous and may be a potential contributor to the Arctic regional climate.

1. Introduction

In the context of global warming, the Arctic temperature has been increasing at a rate higher than the global average in recent decades, which is the so-called “Arctic Amplification” effect (Serreze et al., 2009; Serreze and Francis, 2006). Although the increase of greenhouse gases concentrations was an important driver of the Arctic and global warming, the underlying cause of Arctic amplification remained uncertain as Arctic warming and ice cap melting were also associated with changes in surface albedo, aerosol radiative forcing, cloud cover, atmospheric water vapor content, seawater temperature, and etc. (Screen and Simmonds, 2010; Gillett et al., 2008). The magnitudes of direct radiative forcing of Arctic aerosols were closely related to the origin of aerosol and its transport and deposition (Quinn et al., 2008). During the long transport of aerosols to the Arctic, the solar radiation could be absorbed or scattered by some components in the aerosols (black carbon, sulfate, etc.), which led to a decrease of the amount of solar radiation reaching the surface. However, this cooling effect may be diminished by the decrease of Arctic aerosol concentrations in recent decades (Gagne et al., 2017; Breider et al., 2017). On the other hand, aerosol-radiation interactions also contributed to Arctic warming in the following ways. Firstly, absorbing aerosols at low latitudes could enhance the latitudinal gradient of temperature, thus enhancing heat transport from other regions to the Arctic (Sand et al., 2013b; Sand et al., 2013a); Secondly, absorbing aerosols absorbed solar radiation and warmed the Arctic atmosphere while the surface was cooled, which enhanced atmospheric stability and constrained the diffusion of air pollutants (Blanchet and List, 2010; Koch and Del Genio, 2010; Brock et al., 2011); Thirdly, deposition of absorbing aerosols onto snow and ice could reduce the surface albedo of the Arctic and thus led to local warming. Besides, the formation of mixed-phase clouds in the Arctic were found related to low concentrations and acid coating of dust particles based on both global and parcel model simulations (Fan, 2013). Overall, direct and indirect radiative forcings caused by aerosols had significant impacts on the Arctic climate as demonstrated by the model simulation results (Shindell and Faluvegi, 2009; Flanner, 2013). In addition to the impact of absorbing aerosols on the Arctic climate, the snow-albedo feedback and cloud-albedo feedback in Central Siberia significantly regulated the variation of dust emissions in spring over the Gobi Desert (Liu et al., 2018).

Due to the sparse human activities in the Arctic, most of the air pollutants originated from the middle and lower latitudes, e.g., Eurasia, Siberia, North America, and Southeast Asia. Eurasia was the main source area for the lower Arctic altitudes and the higher Arctic altitudes was mainly influenced by South and Central Asia (Qi et al., 2017; Fisher et al., 2011; Sharma et al., 2013; Stohl, 2006). Di Pierro et al. (2011) and Huang et al. (2015a) both used ground-based lidar data and satellite remote sensing images to demonstrate that aerosols from China can be transported to the Arctic within 4-6 days. Similarly, Di Biagio et al. (2018) found that aerosols in the high Arctic north of Svalbard from October, 2014 to June, 2015 were mainly from Russia. Warneke et al. (2010) found that forest fires in Russia strongly affected air pollutant concentrations in the Arctic atmosphere and surface snowpack based on aircraft observations and numerical simulation. Marelle et al. (2015) investigated a long-transport event from Europe to the Arctic in April, 2008 and estimated a maximum shortwave radiation of 3.3 W m^{-2} at the top of the atmosphere, yielding a significant local warming effect. Sobhani et al. (2018) applied the WRF-STEM (Weather Research and Forecasting - sulfur transport and deposition model) model to study the long-range transport of aerosols to the Arctic and calculated the contribution of various anthropogenic and biomass burning emissions. Europe and China were found as the main source regions of Arctic black carbon, contributing about 46% and 25% in the middle and upper troposphere, respectively.

Different from black carbon, dust had a much larger geographic influencing coverage due to that dust particles were usually accompanied with strong winds. Although a number of studies focused on local or regional dust in the Arctic (Ferrero et al., 2019; Ranjbar et al., 2021; Dagsson-Waldhauserova et al., 2019), the long-range transport of dust to the Arctic has been frequently observed. Asian dust can be transported across the Pacific Ocean to reach North America and even the Arctic (Wang et al., 2018b; Guo et al., 2017). Zwaaftink et al. (2016) combined a Lagrangian particle dispersion model FLEXPART (FLEXible PARTicle dispersion model) and surface particle concentration observations to simulate the global dust emissions. It was found that the instantaneous radiative forcing in the Arctic caused by dust was also dominated by Asia and Africa. In addition, the deposition of dust on snow was responsible for almost all instantaneous radiative forcing at the bottom of the atmosphere (Kylling et al., 2018).

Although both observational and modeling studies showed a persistent source of the Arctic dust from Asia (Fan, 2013; Ginoux et al., 2012), the transport pathways were seldom explored. Huang et al. (2015b) revealed an unreported transport path of Asian dust to the Arctic and estimated its transport duration. In this study, the frequency of dust from East Asia that had the capability to be transported to the Arctic was estimated. Two typical dust transport pathways to the Arctic were investigated based on a synergy of remote sensing data and Arctic monitoring data. The evolutions of aerosol optical properties during the long-range transport were analyzed. Finally, the potential impact of absorbing aerosol on the decrease of surface albedo was quantified.

2. Data and Methodology

2.1. Receptor sites in the Arctic

Two Arctic monitoring sites were chosen as the investigated receptors (Figure 1).They are almost the most northern sites in the Arctic Circle and located in the remote regions where human activities are negligible. Thus, the long-range transported particles can be easily discerned. One site is Barrow (71.32°N, 156.61°W) located in the northernmost part of the Alaska region of USA. It is surrounded by the Arctic Ocean on three sides and has a large ice cap. Barrow is characterized of a cold and dry climate and covered by snow and ice all year round with an average annual temperature of about -11°C (Dong et al., 2010). In winter, the frequency of northerly air currents was high. The average surface temperature reached as low as -25°C in January and February and most of the snowfall occurred at the end of February. Since April, the invasion of warm and moist air masses from the North Pacific Ocean began to prompt the snowpack in Alaska to melt (Stone et al., 2002). This site is managed by Earth System Research Laboratory of National Oceanic and Atmospheric Administration.

The other site is Alert (82.50°N, 62.34°W) in the Nunavut region of Canada, the northernmost permanent human settlement in the world. This site is located about 500 km north of Greenland, near the North Pole and far from any industrial emissions. It is very cold due to the long-lasting polar night with four months in a year. The average temperature was below -30°C from December to March and the average annual temperature was -17.9°C (Weijers et al., 2017). This site is managed by Environment Canada.

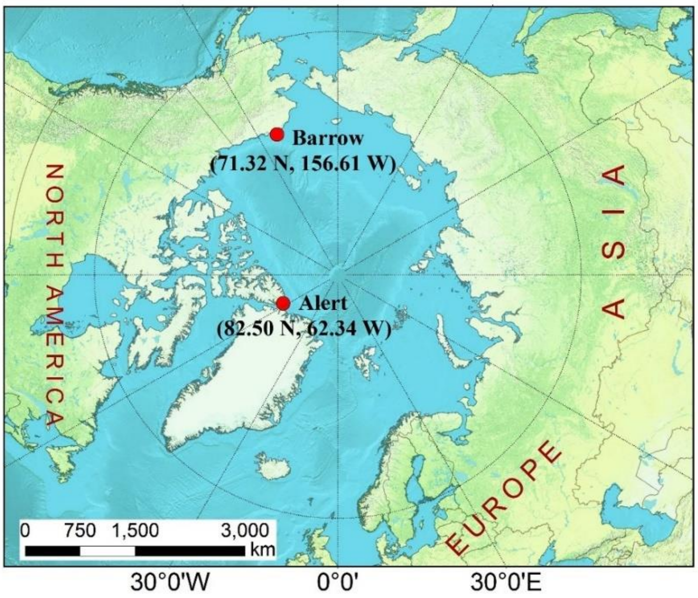

Figure 1. Two receptor sites (Barrow and Alert) in the Arctic. The map is created by ArcGIS 10.2.

2.2. Aerosol measurements

Particles at Barrow and Alert were measured by the three-wavelength (450, 550, and 700nm) Integrating Nephelometer (Model 3563). The nephelometer measured the angular integral of light scattering and Beer-Lambert Law was applied to calculate the light extinction. In this study, the measurement results at 550nm were used. Aerosol absorption was measured by a filter absorption photometer. The aerosol absorption coefficients were obtained at three wavelengths of 467, 530, and 660nm. The measurement results at 530nm were used. Aerosol Robotic Network (AERONET) established a global observational network of columnar aerosol optical properties based on Cimel-31 Sun Photometers (Holben et al., 1998). Key parameters of aerosol optical properties were retrieved at 440 nm, 670 nm, 870 nm, and 1020 nm, respectively. The quality-assured level 2.0 data were used. The AD-Net (Asian dust and aerosol lidar observation network) operated by National Institute for Environmental Studies (NIES) established a lidar network of dual-wavelength depolarization lidars (Model: L2S-SM II), aiming to obtain the four dimensional distributions (sites/time/height/aerosol properties) of aerosol particles in East Asia (Shimizu et al., 2017). The lidar could measure backscattering coefficients and the depolarization ratio at the wavelength of 532 nm. The lidar continuously operated with 15 min intervals and 30m vertical resolution.

In addition to the ground-based sites, remote sensing from space was used to provide widespread spatial information of aerosols. The MODIS (Moderate-resolution Imaging Spectroradiometer) Level-3 aerosol products (1° × 1°) were obtained from NASA’s Giovanni (https://giovanni. gsfc.nasa.gov/giovanni/). Aerosol optical depth (550nm) data was based on the Dark Target (Levy et al., 2007) and Deep Blue (Hsu et al., 2013) algorithm and Angström exponent (0.412-0.47nm) data was based on the Deep Blue algorithm. The CALIOP (Cloud-Aerosol Lidar with Orthogonal Polarization) Lidar onboard the CALIPSO (Cloud-Aerosol Lidar and Infrared Pathfinder Satellite Observation) satellite provided global data on aerosol and cloud layers with a horizontal and vertical resolution of around 5km and 60m. Track scale vertical aerosol profiles were derived. In addition, major aerosol subtypes can be identified, including dust, smoke, clean continental, polluted continental, clean marine, and polluted dust (Omar et al., 2009).

2.3. Air mass trajectories modeling

To track the possible source regions of airborne particles, HYSPLIT4 (HYbrid Single-Particle Lagrangian Integrated Trajectory) was run online at the NOAA (National Oceanic and Atmospheric Administration) ARL (Air Resource Laboratory) READY (Real-time Environmental Applications and Display sYstem) Website (http://www.arl.noaa.gov/ready/hysplit4.html). The HYSPLIT model is a complete system for calculating simple air mass backward trajectories, in addition to dispersion and complex deposition simulations (Draxier and Hess, 1998). The meteorological input data used in the model were obtained from the National Center for Environmental Prediction's (NCEP) global data assimilation system (GDAS) with a horizontal resolution of 0.5° x 0.5°.

2.4. Snow albedo modeling

The Snow–Ice–Aerosol–Radiative (SNICAR) model was used to simulate the impact of impurity (e.g. dust, black carbon, and volcanic ash) on the surface albedo of snow and ice (Flanner et al., 2007). The application of the SNICAR model required inputs such as snow grain effective radius, snowpack thickness/density, surface albedo, the concentrations of impurities in snow. The effective grain sizes of snow ranged from 100 μm for fresh clean snow to 1500 μm for aged snow and granular ice. Table 1 lists the parameters considered for SNICAR in this study. The parameters of snow were derived from field measurements at Barrow in April, 2015 (Dou et al., 2017) and near

Alert in February and April, 2000 (Domine et al., 2002). The estimation of impurities concentrations in snow will be presented in Section 3.7.1.

Table 1. The input parameters in the SNICAR model

Parameters	Barrow	Alert
Incident radiation	Direct	
Surface spectral distribution	Summit Greenland, clear-sky	
Snow grain effective radius (μm)	180(Dou et al., 2017)	500（0.1-1.5mm)(Domine et al., 2002)
Snowpack thickness (m)	0.35(Dou et al., 2017)	0.4(Domine et al., 2002)
Snowpack density (kg/m3)	350(Dou et al., 2017)	300(Domine et al., 2002)
Albedo of underlying ground	0.73（300-700nm）0.33（700-5000nm）(Dou et al., 2017)	

3. Results and Discussion

3.1. Overview of dust events in China from 2011-2015

Table 2 summarizes the occurrence frequency and duration of dust events in the dust source regions of China during 2011-2015 recorded by China's Sand-dust Weather Almanac (Cma, 2013, 2014, 2015, 2016, 2017). A total of 50 dust events occurred, which were categorized into three types, i.e., floating dust, dust storm, and severe dust storm. Among them, the occurrence frequency of floating dust reached 36, accounting for 72% of the total dust events. On average, floating dust occurred about 7 times a year with a total duration of 61 days. The occurrence frequencies of dust storm and severe dust storm events were both 7 times with the total duration of 18 days. Compared with 2000-2010, the frequency of dust storm and severe dust storm events during the last five years decreased significantly, while that of floating dust increased.

Table 2. Summary of dust weather conditions in China during 2011 – 2015

Year	floating dust		dust storm		severe dust storm		Total
	frequency	days	frequency	days	frequency	days	frequency
2011	5	10	1	3	2	6	8
2012	5	10	3	8	2	4	10
2013	9	15	1	2			10
2014	4	8	1	2	2	6	7
2015	13	18	1	3	1	2	15
Total	36	61	7	18	7	18	50

On a seasonal basis (Table 3), the springtime (March-May) was the peak period of dust outbreak in China. 41 dust events occurred, accounting for 82% of the total dust events. Of which, relatively high frequencies of dust storm and severe dust storm events were observed, accounting for 37.5% of the total events in April. This high frequency of dust occurrence in the spring of China was mainly related to the climatic characteristics, geographic conditions, and geological structure of northern China. Strong winds caused by the Inner Mongolia cyclone and cold fronts in spring resulted in the frequent outbreak of dusty weather in northern China. In terms of the geographical dust source areas in China, the source regions of dust included the South Xinjiang basin, central and western Inner Mongolia, central and western Gansu, and northern Shaanxi.

Table 3. Monthly summary of dust days in China during 2011 – 2015

Month	floating dust	dust storm	severe dust storm	total
February	3			3
March	12	1	2	15
April	10	3	3	16
May	7	1	2	10
June	1			1
August	1			1
November	2	2		4

3.2 Transport pathways of Asian dust to the Arctic

In order to investigate the frequency and transport pathways of dust from China to the Arctic, the HYSPLIT trajectory model was applied in this study. Based on the outbreak time and source areas of dust recorded by China's Sand-dust Weather Almanac, 10-15 days forward trajectories starting at typical altitudes of lifted dust (500m, 1000m, and 1500m) were computed for each dust event in China during 2011-2015. If the trajectories entered the Arctic Circle (latitudes higher than 66°34'N), the specific dust event was recorded as one dust long-range transport event from China to the Arctic.

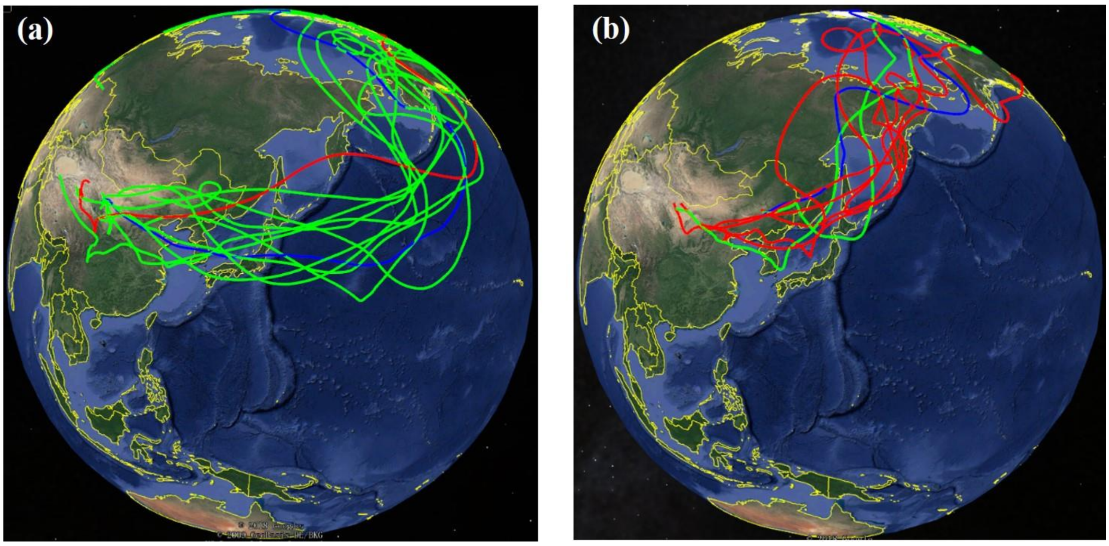

Figure 2. Two common transport pathways of dust originating from China to the Arctic, i.e., (a) the northern China - Korean Peninsula/Japan - North Pacific Ocean – Arctic pathway and (b) the northern China - Korean Peninsula/Japan - Kamchatka Peninsula - East Siberia – Arctic pathway. Red, blue, and green curves represent forward trajectories starting at altitudes of 500m, 1000m, and 1500, respectively. The map is © Google Earth 2019.

Based on this criterion, 38 out of the 50 dust events that originated from China during 2011-2015 had the potential migrating to the Arctic Circle. Among these identified dust events, most occurred in spring with 32 events and the transport duration varied between 4 and 13 days. Two main types of dust transport from China to the Arctic were distinguished in Figure 2. As for Type I (Figure 2a), dust mainly originated from the central parts of Inner Mongolia and central Gansu. It passed through northern China, Korean Peninsula, Japan and the North Pacific Ocean, and finally reached Siberia and the northern part of Alaska. This transport type was characterized of wide geographic coverage, relatively long transport duration (about 7-10 days), and mainly over the open ocean. This was due to the high lifting altitude (mostly over 1500m) over the dust source regions, so particles can be transported to even further areas.

As for Type II (Figure 2b), dust mainly originated from northeast China and western Inner Mongolia, then passing over the Korean Peninsula, northern Japan, Kamchatka Peninsula, and finally reaching East Siberia and its northern areas. Compared to Type I, the Type II transport pathways travelled more over land and had relatively shorter duration of about 4-8 days. This was due to the presence of a low-pressure system over northern Japan in spring, which induced the air masses deflecting northward. In Section 3.4, more details about the low-pressure system will be presented based on case analysis.

More explicit characterizations of the transport pathways from the dust source regions to the Arctic will be discussed later in Section 3.5.

3.3 Two cases of long-range transported dust to the Arctic

Figure 3a shows the time series of scattering coefficients (σ_{sp}) of PM_1 and PM_{10} at 550 nm at Barrow during April 17-21, 2015. The scattering coefficients stayed at low levels from the early morning of April 17 to the evening of April 18, which were similar to the annual average values at Barrow in 2015 (4.8 Mm^{-1} and 8.1 Mm^{-1} for PM_1 and PM_{10}, respectively). Since the early morning of April 19, both $\sigma_{sp}(PM_1)$ and $\sigma_{sp}(PM_{10})$ climbed simultaneously, indicating the invasion of air pollutants. At 15:00 on April 19, $\sigma_{sp}(PM_1)$ reached relatively high value of 19.8 Mm^{-1} and was still close to that of PM_{10} with the $\sigma_{sp}(PM_1)/\sigma_{sp}(PM_{10})$ ratio of 0.82, indicating fine particles dominated during this period. Afterwards, $\sigma_{sp}(PM_{10})$ continued to increase until it reached the maximum value of 42.2 Mm^{-1} at 4:00 on April 20, more than 5 times of its annual average. The mean $\sigma_{sp}(PM_1)/\sigma_{sp}(PM_{10})$ ratio during 14:00, April 19 - 12:00, April 21 decreased to 0.47 ± 0.10, obviously indicating the enrichment of coarse particles. This episode is defined as CASE I.

Figure 3b shows the time series of scattering coefficients of PM_1 and PM_{10} at 550 nm at Alert from March 13 to 19, 2013. The annual average $\sigma_{sp}(PM_1)$ and $\sigma_{sp}(PM_{10})$ at Alert was 4.2 Mm^{-1} and 6.0 Mm^{-1}, respectively, slightly lower than those observed at Barrow. From 0:00 on March 14, $\sigma_{sp}(PM_1)$ and $\sigma_{sp}(PM_{10})$ started to increase and reached the maximum values of 18.6 Mm^{-1} and 32.3 Mm^{-1} at 0:00 on March 15, which were more than 4 and 5 times of their annual average, respectively. The mean $\sigma_{sp}(PM_1)$/

$\sigma_{sp}(PM_{10})$ ratio during 11:00 on March 14 to 7:00 on March 18 was 0.61 ± 0.03, also indicating the enrichment of coarse particles. This episode is defined as CASE II.

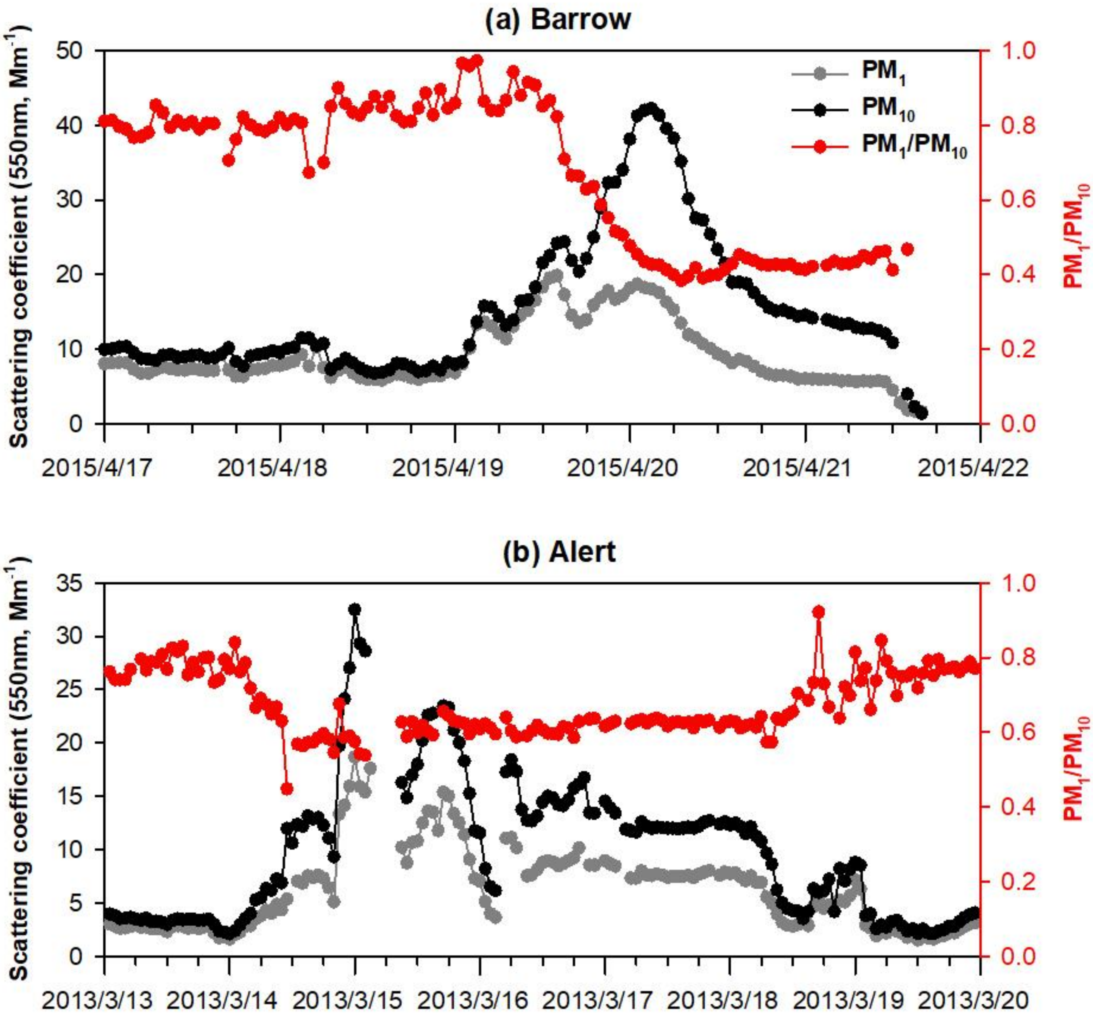

Figure 3. (a) Time series of hourly scattering coefficients of PM_1 and PM_{10} at 550 nm and the ratio of PM_1/PM_{10} at Barrow during April 17-21, 2015. (b) The same but for Alert during March 13 to 19, 2013.

In comparison, the pollution during CASE I lasted for a relatively short period of about 2.5 days while had higher peak values of $\sigma_{sp}(PM_{10})$ than CASE II, indicating that CASE I was subject to stronger long-range transport and more significant variations of synoptic conditions. The pollution during CASE II lasted for nearly four days, suggesting relatively weak cleanup processes of the air pollutants. As for the $\sigma_{sp}(PM_1)$/

$\sigma_{sp}(PM_{10})$ ratio, it was much lower in CASE I than that in CASE II. This indicated the intrusion of coarse particles was more intense during CASE I, which could be related to various factors such as the emission source regions, transport pathways, and evolution of particles. In the next section, the transport pathways of the two cases above were validated by using backward trajectory analysis and remote sensing from both space and ground-based observations.

3.4 Identification of dust long-range transport pathways

To determine the sources and transport pathways of the two Arctic pollution events, the HYSPLIT model was applied to compute the air masses transport trajectories. Figure 4a shows the 7-days backward trajectory simulated at an altitude of 6 km above Barrow starting from 04:00 on April 20, 2015 (CASE I). The different segments of the trajectory were colored to represent the continuous dates. On 14-15 April, air masses originated from the Taklamakan and Gobi deserts in China, then passed over East Asia, Siberia of Russia, and the Pacific Ocean, and finally reached Barrow about 6 days later. The geopotential height fields based on the NCEP reanalysis data are plotted in Figure 4c-4f to verify the dust transport path. On April 16, a low-pressure trough over Northeast China caused the eastward air masses to turn northward. On April 17, the air masses followed the high-pressure ridge over eastern Russia and entered the North Pacific. Then its direction was again deflected by a low-pressure system near the Bering Strait on April 18 and 19, finally reaching Barrow on April 20.

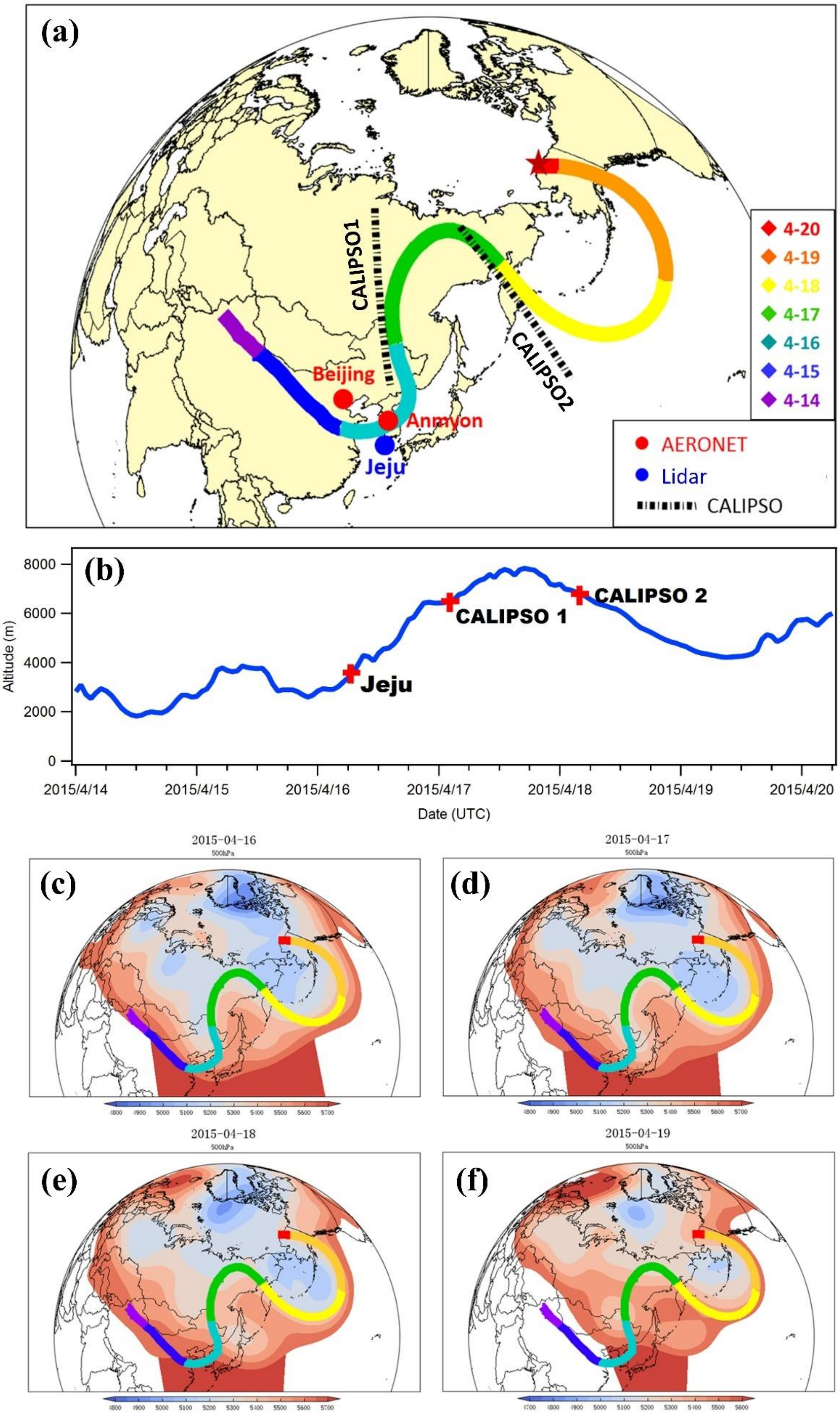

Figure 4. (a) The 7-days backward trajectory simulated at an altitude of 6 km

above Barrow starting from 04:00 on April 20, 2015. The locations of AERONET, Lidar sites, and CALIPSO tracks nearby the trajectory are plotted. (b) The height of the trajectory along the transport path. The height and time of dust layers observed by lidars and CALIPSO in Figure 4a are indicated by the red plus symbols. (c-f) Daily geopotential height fields (500 hPa) from the NCEP reanalysis data

Figure 5a shows a typical backward trajectory simulated at an altitude of 4 km above Alert on March 14, 2013 (CASE II). On March 7, air masses travelled over the Gobi Desert on the border between Mongolia and the north of China, then passed over Korea and Japan, and directly entered the Pacific Ocean. Afterwards, it kept moving northward across the Arctic Ocean and reached Alert on March 14. Based on the geopotential heights (Figure 5c-5h), a low-pressure system was observed over the eastern coast of Russia and kept moving to the southeast from March 7 to 11. On March 11, the low-pressure system moved over the Sea of Okhotsk in Russia and turned to be stronger, causing the air masses deflect and follow the geopotential height contours all the way north to Alert.

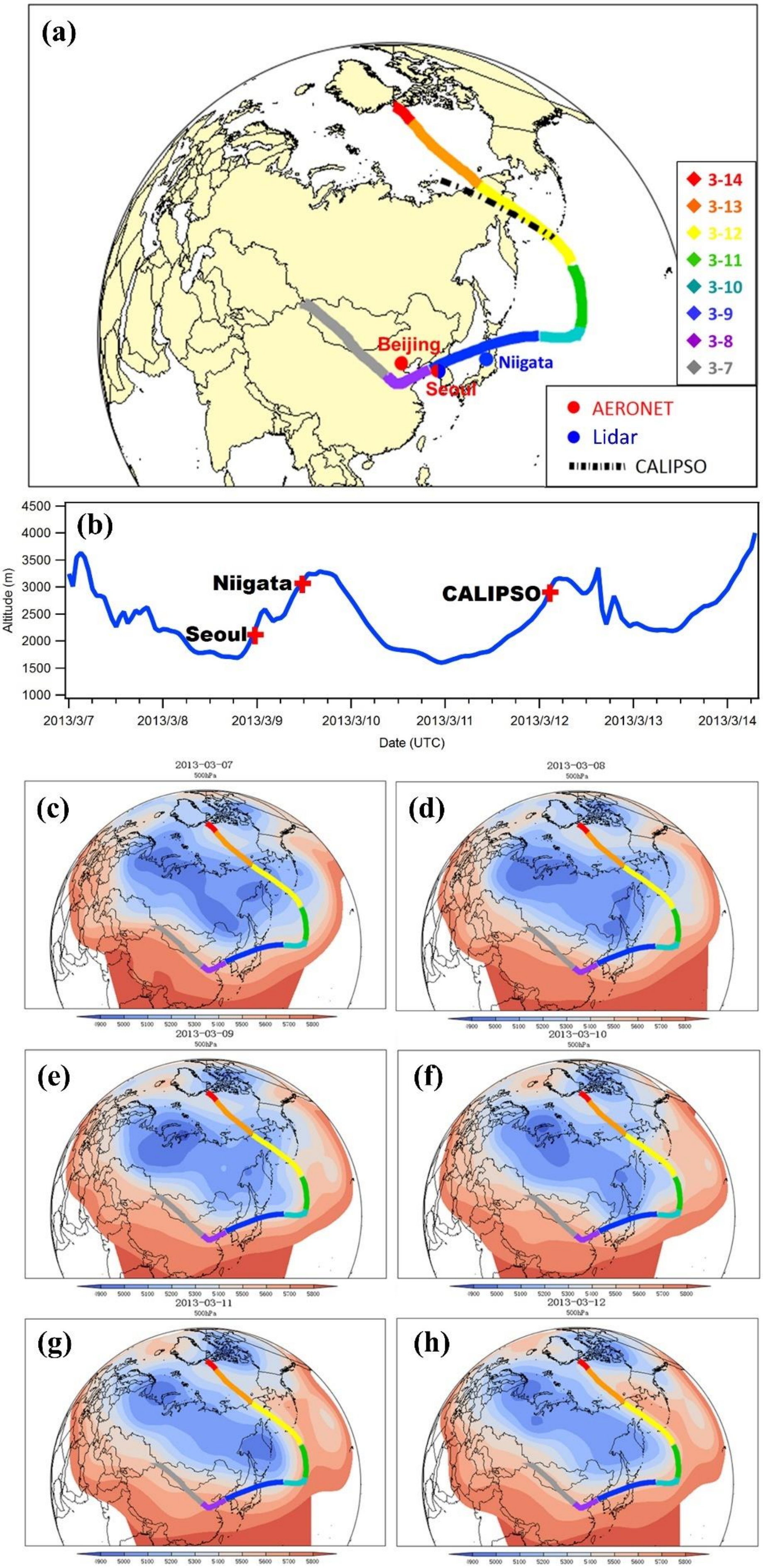
(a)
3-14
3-13
3-12
3-11
3-10
3-9
3-8
3-7
Beijing
Seoul
Niigata
AERONET
Lidar
CALIPSO
(b)
Niigata
Seoul
CALIPSO
Altitude (m)
4500
4000
3500
3000
2500
2000
1500
1000
2013/3/7
2013/3/8
2013/3/9
2013/3/10
2013/3/11
2013/3/12
2013/3/13
2013/3/14
Date (UTC)
2013-03-07
500hPa
(c)
2013-03-08
500hPa
(d)
2013-03-09
500hPa
(e)
2013-03-10
500hPa
(f)
2013-03-11
500hPa
(g)
2013-03-12
500hPa
(h)
4900 5000 5100 5200 5300 5400 5500 5600 5700 5800

Figure 5. Same as Figure 4 but for CASE II.

3.5 Verification of dust transport pathways based on satellite and ground-based observations

Although the air mass transport pathways of the two Arctic coarse particle pollution cases were visualized based on trajectory modeling, whether dust particles were indeed present in the air masses has not been confirmed. In this section, the aerosol optical properties along the transport pathway were explored using both ground-based observations (AERONET and AD-Net) and satellite inversion data (CALIPSO). In Figure 4a and 5a, the red dots denoted the AERONET sites, which observed columnar aerosol optical properties. The blue dots denoted the AD-Net sites, which observed vertical profiles of aerosol extinctions and particle morphology information. The black dashed lines represented the orbits of CALIPSO profiles, which were used to supplement the aerosol information in the blank areas without available ground-based observations. The validation results of the two cases are described separately as below.

(i) CASE I

Figures 6 shows the aerosol optical properties of two AERONET sites, i.e., Beijing (China) and Anmyon (Korea), which were located nearby the air mass transport pathway in CASE I (Figure 4a). AE (Angström exponent) is a parameter of characterizing the particle size. The smaller AE represents the larger particle size, and vice versa. In general, AE < 1 suggested the dominance of coarse particles, which were usually associated with dust or sea salts. While AE > 1 suggested the dominance of fine particles, which derived from anthropogenic emissions and biomass burning.

As shown in Figure 6a, AOD over Beijing doubled from about 1.0 at around 0:00 on April 15 to nearly 2.0 at around 6:00, while AE (440-870nm) remained below 0.5. When the air masses passed over Anmyon, Korea, AOD was about 0.4 at 8:00 on April 16 (Figure 6b). AOD at Anmyon was much lower compared to Beijing, which should be due to the removal process during the transport and lower local emissions at Anmyon. Similarly, AE at this site was low below 0.4 and it slightly increased to above 0.5 after 8:00. As a whole, the observation of high AOD and low AE at both sites indicated that the air masses contained abundant coarse dust aerosols.

Figure 6c shows the vertical profiles of aerosol optical properties over Jeju Island, Korea. The depolarization ratio represents the degree of particle approximation to a sphere in the range of 0 - 1. The depolarization ratio of a spherical object is equal to 0, and vice versa (Mishra et al., 2010). Since dust aerosols were irregularly shaped particles, the depolarization ratio of dust aerosols usually ranged between 0.2 and 0.3. As for the intense dust storm events, the depolarization ratio of particles could reach over 0.4 (Liu et al., 2003). High extinction coefficients and depolarization ratios between 0.1 and 0.3 at around 4 km over Jeju in the early morning of April 16, 2015 were observed. By comparing the simulated height of the air mass backward trajectory and the observed plume height over Jeju, good agreement was found (Figure 4b), corroborating the same origin of the Arctic pollution and the Asian downstream dust plumes.

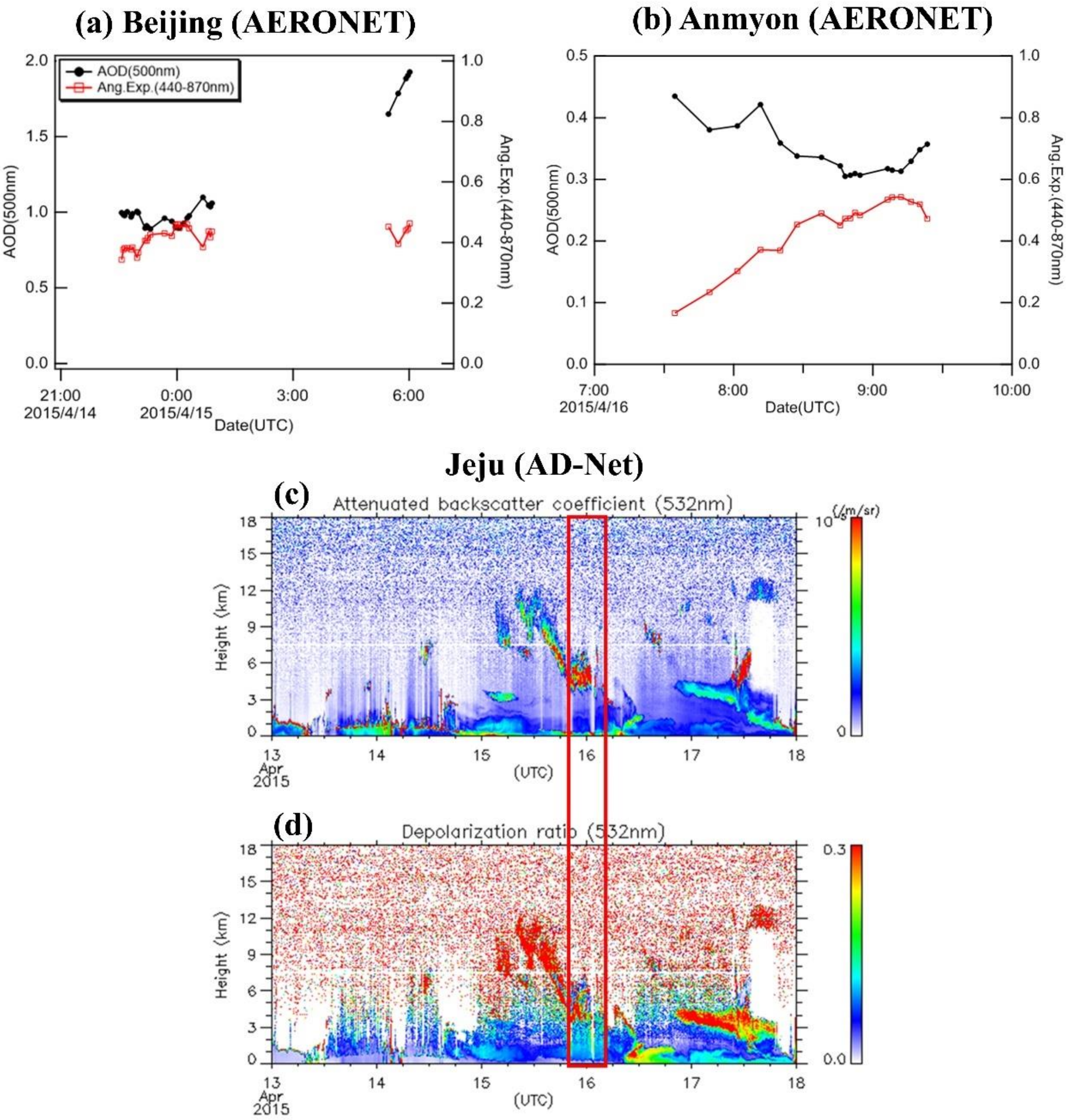

Figure 6. Aerosol optical properties observed at ground-based sites during CASE I. (a) AOD (500nm) and Angström exponent (440-870nm) at the Beijing AERONET site. (b) AOD and Angström exponent at the Anmyon AERONET site. Vertical profiles of (c) backscattering coefficient and (d) depolarization ratio at the Jeju AD-Net site. The red rectangle denotes the time when dust passed over the site. Clouds are screened and represented by the blank pixels.

After April 16, the dust plume moved towards Russia and the North Pacific. Due to the lacking of ground-based observations in this region, CALIPSO inversion products were used to fill in these blank regions. At about 5:00 UTC on April 17, 2015, over the northeastern part of Russia (54.19°N, 122.17°E), CALIPSO observed an aerosol layer, about 5 km above the ground. This height was generally consistent with that of the simulated backward trajectory (Figure 4b) and the plume was identified as a mixture of dust, polluted dust, and other types of aerosols (Figure 7). At 2:00 UTC on April 18, CALIPSO observed a similar mixed layer of dust, polluting dust, and lifted smoke at 4-6 km over the Kamchatka Peninsula in Russia (Figure 7). Compared to the previous day, the lifted smoke was more abundant, suggesting that smoke aerosols from forest fires may have been mixed with the air masses passed over Russia.

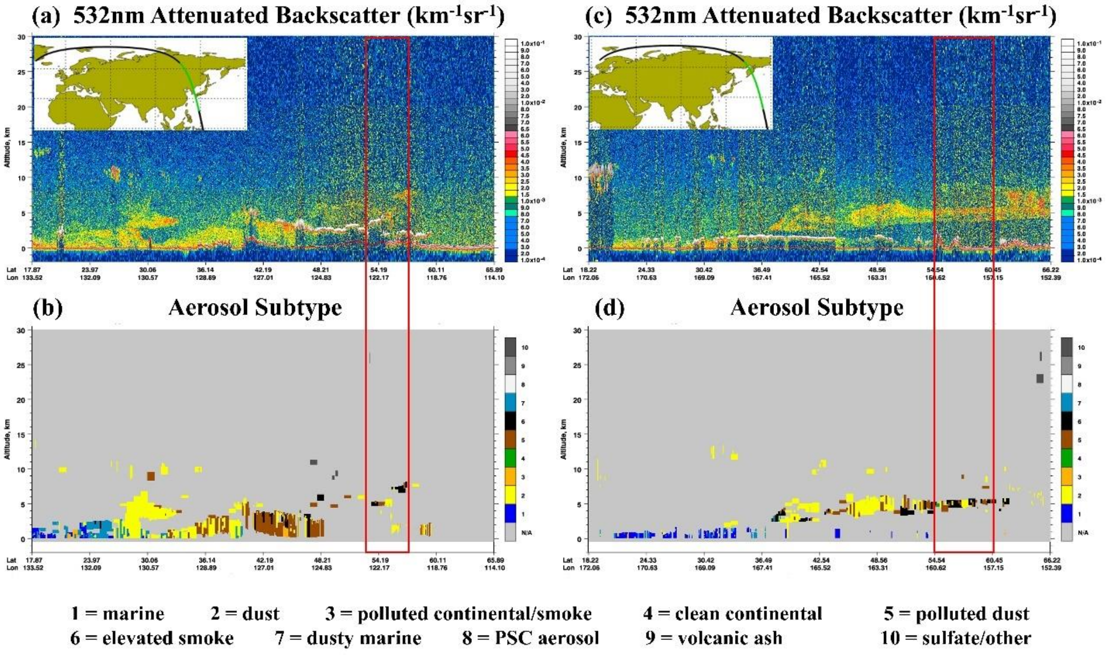

Figure 7. CALIPSO profiles of aerosol backscattering coefficients and identified aerosol types on April 17 (a-b) and 18 (c-d), 2015. The red rectangles denote the regions as indicated by the CALIPSO tracks in Figure 4a.

(ii) CASE II

Figure 8 shows the available ground-based observations close to the transport pathway during CASE II. At the Beijing AERONET site, at 3:00 UTC on March 8, 2013, AOD was 0.73 while AE was 0.47. This was indicative of the dominance of dust particles. Afterwards at 8:00, AOD increased more than twice and approached 2.5, while AE also increased to more than 0.9, indicating that the dust in CASE II was more mixed with fine particles than CASE I.

From 0:00 to 6:00 UTC on March 9, 2013, observed AE at the Seoul AERONET site decreased to a low level of about 0.6 and increased to around 1.0 for several hours. This process was accompanied by a continuous increase of AOD, reaching a maximum of 1.15. In addition, the vertical profiles of the aerosol optical properties in the early morning of March 9 indicated a 1-2 km thick dust layer at altitudes of 1-3 km height over Seoul (Figure 8c), which was in good agreement with the height of the backward trajectory (Figure 5b). Figure 8d shows the lidar vertical observations in Niigata, Japan. A 1-2km thick dust layer at altitudes of 2 – 4km was also observed at 9:00-12:00 UTC on March 9. The heights of the dust layers observed from lidars were also in good agreement with the time and height of the simulated backward trajectory as shown in Figure 5b.

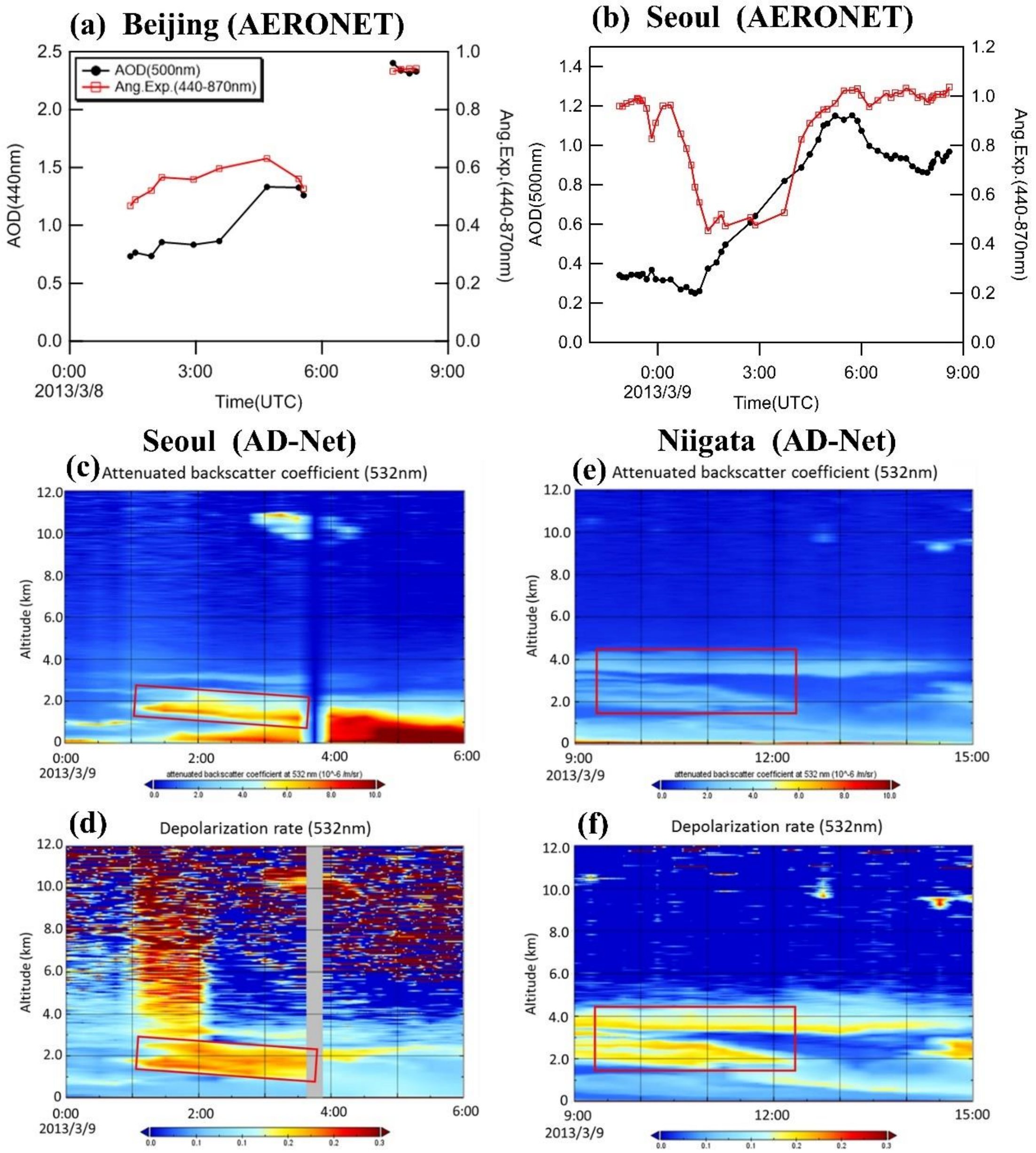

Figure 8. Aerosol optical properties observed at ground-based sites during CASE II. (a) AOD (550nm) and Angström exponent (440-870nm) at the Beijing AERONET site (b) AOD and Angström exponent at the Seoul AERONET site (c-d) Vertical profiles of backscattering coefficient and depolarization ratio at the Seoul AD-Net site (e-f) Vertical profiles of backscattering coefficient and depolarization ratio at the Niigata AD-Net site. The red rectangle denotes the time when dust passed over the site.

Figure 9 shows the aerosol vertical structure observed from CALIPSO over the Bering Sea (51.28°N, 175.96°E - 57.23°N, 172.96°E) on March 12, 2013. At around 2.5 - 4 km, an aerosol layer was evident, consisting of dust and polluted dust, confirming that the aerosols transported to the remote ocean still contained a large amount of dust particles.

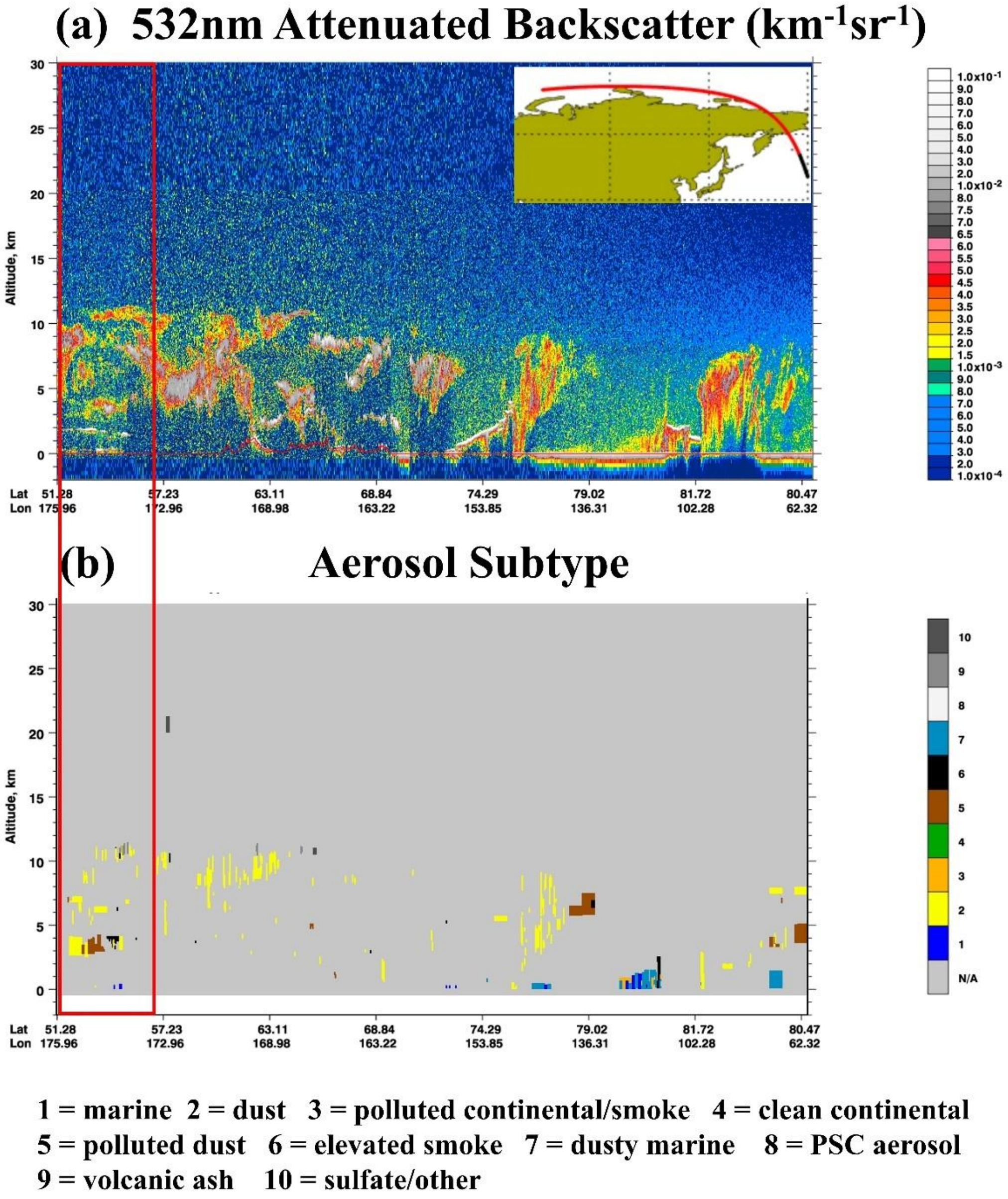

Figure 9. CALIPSO profiles of (a) aerosol backscattering coefficients and (b) identified aerosol types on March 12, 2013. The red rectangles denote the regions as indicated by the CALIPSO tracks in Figure 5a.

By comparing the transport pathways of CASE I and CASE II, CASE I passed over more terrestrial areas, increasing the probability of mixing between dust and air pollutants from anthropogenic emissions. While CASE II travelled more over the open ocean, which was more likely to mix with sea salts. In terms of transport time, the air masses in CASE I took about four days to reach the receptor after getting out of the Asian dust source regions, while the air masses in CASE II took about six days. The longer transport time in CASE II may lead to more deposition of coarse dust particles due to the gravitational effect and other removing processes such as wet scavenging.

3.6 Evolution of aerosol optical properties during long-range transport to the Arctic

In the previous section, it has been well demonstrated that the Arctic air pollution events in both CASE I and CASE II were caused by the long-range transport of Asian dust. However, only a limited observation from ground-based sites and CALIPSO was available for the analysis of aerosol properties. In order to analyze the evolution of aerosols during the transport, MODIS data with a wide spatial coverage was used to quantify the changes of aerosol optical properties.

As shown in Figure S1, MODIS data were analyzed on a daily basis. Since simulated backward trajectories were subject to certain uncertainties (Draxler and Hess, 1998), the rectangular subsection that covered the daily trajectory was extracted to represent the aerosol properties along the transport pathway. Figure 10 compares the mean values of AOD and AE over the daily transport coverage area between the two cases. As shown in Figure 10a, AOD in CASE I exhibited an evidently decreasing trend with time. It averaged 0.86 on April 14, 2015 over the dust source regions, while it was 0.10 at Barrow on April 20, indicating a tremendous AOD decrease of nearly 8 times. In the meanwhile, AE showed an increasing trend (Figure 10b). This indicated that, on the one hand, the high aerosol concentrations from the dust source regions had been significantly eliminated by various physical scavenging processes. In the meantime, local air pollutants could be reduced by the strongly invaded dust (Wang et al., 2018a). On the other hand, dust mixed with fine particles such as black carbon, nitrate, and sulfate and gradually modified the irregular dust particles to be more spheric (Xu et al., 2020).

In contrast, less variation of AOD during the transport was observed in CASE II (Figure 10c). AOD was relatively low over the Gobi Desert on March 7 while the mean AOD even increased to 0.56 - 0.68 from March 8 to 11. As shown in Figure S1b, the eastward movement of aerosol plume was evident. This probably indicated the dust plume had already drifted away from the dust source region, which explained the lower AOD in the source region than the downwind regions. Meanwhile, except for the low value of AE on March 8 (possibly due to the small number of data points as shown in Figure S1b), the mean AE values were above 1.0 on March 7 and 9. This suggested that dust mixed with more fine particles and coarse particles were more removed. Overall, by comparing these two cases, it was evident that different transport routes to the Arctic had divergent effects on the evolution of aerosol optical properties.

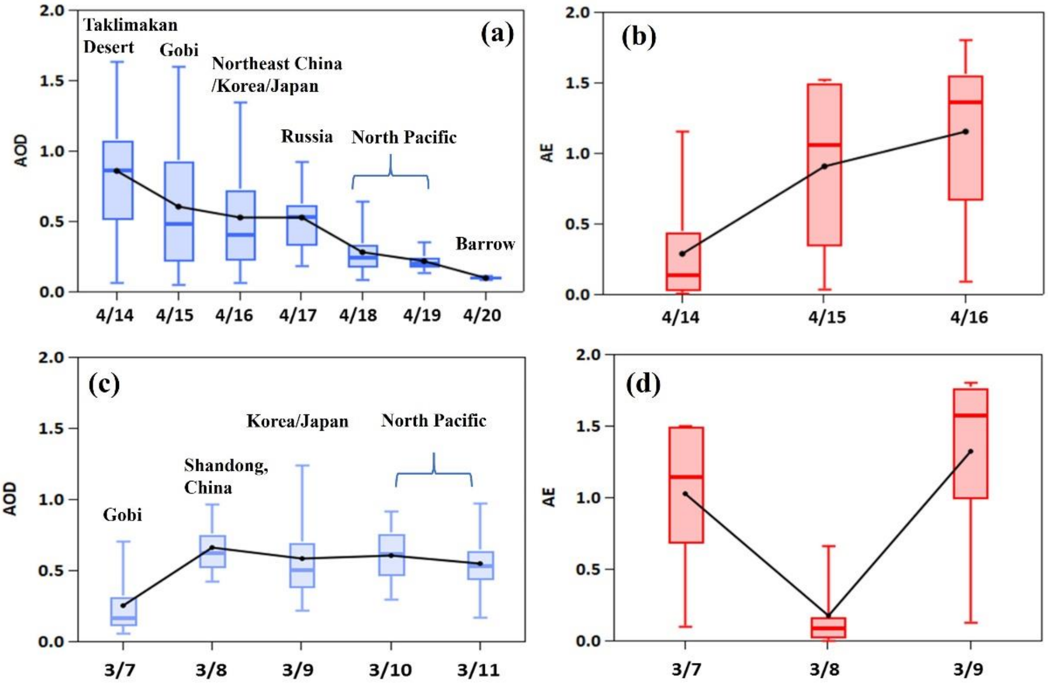

Figure 10. Regional (a) AOD and (b) Angström exponent in CASE I. Regional (c) AOD and (d) Angström exponent in CASE II. The dots and lines inside the boxes represent the mean and median values, respectively; bottom and top of the boxes represent the 25 and 75% limits, respectively; and bottom and top short lines represent the minimum and maximum values, respectively. The geographic region in each day is defined in Figure S1.

3.7 Impact assessment of transported aerosols on the Arctic surface albedo

Surface albedo is an important parameter for energy exchange between the surface and the atmosphere in polar regions. The changes in snow and ice albedos could have important climatic impacts on the polar regions as well as the whole world. Due to the large difference between the multiple scattering effect of snow and ice and absorption effects of absorbing impurities (e.g. black carbon and dust), very small amounts of deposited impurities can lead to a decrease of snow and ice albedo (Zhang et al., 2017). Hansen and Nazarenko (2004) showed that the effect of soot on reducing snow and ice albedo was around 1.5% in the Arctic and 3% in the snow and ice covered areas of the

Northern Hemisphere. Kaspari et al. (2014) showed that black carbon reduced snow and ice albedo by 6-10% relative to pure snow in the Himalayas in winter and spring, and other impurities such as dust even reduced snow and ice albedo by 40 - 42%. In this regard, decreases of snow and ice albedo would cause surface warming, thinning of sea ice, melting permafrost, and consequently sea level rise that may have serious impacts on the global water resources and ecosystems.

In this section, the impacts of the two Arctic pollution events on changing the surface albedo were assessed. The SNICAR snow and ice albedo model was applied to estimate the contributions of dust and black carbon to the reduction of snow and ice albedo.

3.7.1 Estimation of mass concentrations of impurities in snow and evaluation of model performance

In this study, we only considered airborne dust and elemental carbon (EC) as the dominant contributors to the impurities in the Arctic snow and ice. Firstly, the atmospheric concentrations of absorbing aerosols were estimated by using the revised IMPROVE (The Interagency Monitoring of Protected Visual Environments) Equation (Pitchford et al., 2007). It was assumed that airborne dust and EC dominated the scattering of coarse particles and absorption of fine particles, respectively (Eq. 1-2).

$C_{dust} = b_{sca,(PM10 - PM1)} / 0.6,$ (1)

$C_{EC} = b_{abs,PM1} / 10,$ (2)

Of which, the constant 0.6 and 10 (m^2/g) is the mass scattering efficiency and mass absorption efficiency of dust and EC, respectively (Pitchford et al., 2007). Since the concentrations of impurities in snow were required as inputs for the SNICAR model, we estimated them based on the following assumption. Dou et al. (2017) conducted field sampling at Barrow during April and May in 2015 and measured elemental carbon concentration of 3.30 ng/g in the snow sample on April 30, 2015. The airborne elemental carbon concentration was estimated to be 6.25 ng/m^3 on the same day by using the equations above. Thus, the ratio of the particulate matter in the snow versus that in the atmosphere was calculated to be 0.528m^3/g. This ratio was then applied to estimate the concentrations of dust and elemental carbon in snow during the two cases based on the assumption that particulate dust and elemental carbon could be well mixed under the sufficiently long transport duration. Since the cumulative effect of impurities in reducing the surface albedo was not considered in this study, the simulation result by the SNICAR model was considered as the instantaneous surface albedo in the following discussions.

To evaluate the model performance, Figure S2 compares the simulated values of surface albedo and the observations at an ARM (Atmospheric Radiation Measurement) site located at Barrow during 14 – 19, April, 2015. A correlation coefficient of 0.74 was derived, indicating the relatively good model performance on simulating the Arctic surface albedo. However, deviations of simulated values from observations were still found. The bias may derive from the following aspects. First, the concentrations of dust and elemental carbon in snow as inputs for the model were not in-situ measured, as well as for the other input parameters such as snow radius, thickness, and density. Secondly, the simulation only considered the absorbing substances deposited from the atmosphere while the pre-existing impurities in snow and ice were ignored. Last but not the least, impurities such as brown carbon were not included for the simulation.

3.7.2 Comparison of the changes of Arctic surface albedo between two cases

In this section, the impacts of transported particles on the change of surface albedo in both cases were evaluated. Figure S3 shows the time-series of estimated dust and elemental carbon in snow during the two pollution cases. As for CASE I (Figure S3a), the peak time of elemental carbon was about half a day ahead of that of dust. This phenomenon was as similar as some other dust events that anthropogenic air pollutants were ahead of dust pushed by the cold front (Guo et al., 2004; Wang et al., 2018a). In regard of the variations of pollutants, four representative moments were selected, i.e., 0:00 on April 18 (the beginning of pollution), 13:00 on April 19 (the peak time of elemental carbon), 3:00 on April 20 (the peak time of dust), and 15:00 on April 21 (the end of pollution). As for CASE II (Figure S3b), the estimated concentrations of impurities in snow stayed at relatively low levels and varied less strongly compared to CASE I. We chose 12:00 on March 14 (the beginning of pollution), 17:00 on March 15 (the peak time of dust), and 13:00 on March 18 (the end of pollution) for the analysis.

By using the SNICAR model, the effects of dust, elemental carbon, and combination of dust and elemental carbon on the surface albedo were separately assessed. As shown in Table 4, the reduction of surface albedo caused by long-range transported Asian light-absorbing pollutants ranged from 0.35% to 2.63%, which were consistent with previous studies. For instance, Dou et al. (2017) calculated a 1.6-5.1%

reduction in snow and ice albedo caused by dust and black carbon at Barrow from late April to May 2015, with a 5-10 fold increase in pollutant concentrations compared to the pre-April period due to the snowmelt period during that time. Zhang et al. (2017) calculated that dust and black carbon reduced snow and ice albedo by 0.72-1.00% on glaciers in the southeastern Tibetan Plateau in June 2015. In CASE I, the highest concentration of elemental carbon in snow reached more than 72 ng/g, which could reduce the albedo by 1.47%. And the highest concentration of dust reached more than 37 μg/g, which could reduce the albedo by 2.26%. During this pollution event, the combined effect of dust and elemental carbon significantly reduced the snow and ice albedo by 2.28%. In CASE II, elemental carbon concentrations were much lower than CASE I and its effect on albedo was below 0.40%, while dust can reduce albedo up to 1.87%. The combined effect of dust and elemental carbon reached more than 2% compared to the pure snow condition.

Table 4. Simulated changes of albedo due to dust, elemental carbon, and combination of dust and elemental carbon (SA represents the simulated surface albedo of pure snow)

Time (UTC)	BC snow (ng/g)	Dust snow (μg/g)	SA Pure	SA+EC	SA+Dust	SA+EC & Dust	EC (%)	Dust (%)	EC&Dust (%)
				Barrow					
2015/4/18 0:00	24.31	8.31	0.7990	0.7901	0.7915	0.7852	1.12%	0.94%	1.73%
2015/4/15 15:00	72.14	21.39	0.8392	0.8270	0.8300	0.8218	1.47%	1.10%	2.07%
2015/4/20 3:00	21.16	37.11	0.8143	0.8077	0.7959	0.7929	0.83%	2.26%	2.63%
2015/4/21 15:00	6.08	1.93	0.8379	0.8361	0.8365	0.8350	0.22%	0.17%	0.35%
				Alert					
2013/3/14 13:00	7.75	10.77	0.7995	0.7964	0.7912	0.7891	0.39%	1.04%	1.30%
2013/3/15 17:00	7.37	20.74	0.7923	0.7892	0.7775	0.7758	0.40%	1.87%	2.08%
2013/3/18 13:00	6.52	3.68	0.7956	0.7929	0.7921	0.7899	0.34%	0.44%	0.72%

As discussed above, the concentrations of dust and elemental carbon were relatively higher in CASE I, hence the resulting effects on snow and ice albedo were more obvious. On the one hand, the transport time in CASE I was shorter and the particulate matters were scavenged less along the transport. On the other hand, the air masses in CASE I passed over a large number of terrestrial areas, including northeast China and Siberia. Fine particles from anthropogenic emissions and biomass burning in Siberia mixed with dust and transported to Barrow together, making the elemental carbon at the receptor significantly higher. As for CASE II, the receptor site at Alert is a higher latitudinal area, which was much less affected by local anthropogenic activities. In addition, the transport pathway of CASE II was mostly over the open ocean with longer duration. This finally induced much lower air pollutant concentrations and weaker impact on the reduction of surface albedo.

4. Conclusions

In this study, the long-range transport of Asian dust to the Arctic was investigated. During 2011-2015, 50 dust events in China were recorded, of which 38 dust events had the capability to reach the Arctic based on the air mass trajectory simulation. Two main transport routes were identified. One typical transport type was characterized of wide geographic coverage, long transport duration (generally 7-10 days), and mainly marine transport due to the high lifting altitude of dust particles (mostly over 1500m) over the dust source regions. The other typical transport type was characterized of dust transport mostly over land with relatively short duration of about 4-8 days. This was due to the presence of a low-pressure system over northern Japan in spring, which induced the air masses deflecting northward.

Two typical coarse particle dominated cases observed in the Arctic were specifically investigated, i.e., one at Barrow in April 2015 (CASE I) and the other one at Alert in March 2013 (CASE II), respectively. Based on the air mass trajectory simulation, in CASE I, dust originated from the Taklamakan and Gobi deserts in China, then passed over East Asia, Siberia of Russia, and the Pacific Ocean, and finally reached Barrow. In CASE II, dust originated from the Gobi Desert, then passed over Korea and Japan and directly entered the Pacific Ocean, and finally moved northward across the Arctic Ocean and reached Alert.

The dust transport pathways during both cases were verified based on a synergy of NCEP reanalysis data (geopotential height fields), ground-based observations (AERONET aerosol columnar properties and lidar aerosol profiles), and satellite products (CALIPSO profiles). The passing time and height of the dust plume based on trajectory simulation coincided very consistently with various observations. The evolution of aerosol optical properties during the transport was assessed by using the large-scale MODIS data. In CASE I, AOD showed a significant decreasing trend while Angström exponent showed an increasing trend from the dust source region to the receptor. In contrast, AOD varied much less significantly in CASE II. It was evident that different transport routes to the Arctic had divergent effects on the evolution of aerosol properties.

The SNICAR snow and ice model was applied to simulate the impact of impurities on the reduction of surface albedo in the Arctic during the two cases. The concentrations of dust and elemental carbon in snow were estimated and the effects of dust, elemental carbon, and combination of dust and elemental carbon on snow and ice albedo were separately quantified. The reduction of snow and ice albedo caused by long-range transported Asian light-absorbing pollutants ranged from 0.35% to 2.63%. This study highlighted that the long-range transport of Asian dust to the Arctic was ubiquitous and its impact on changing the radiative forcing and regional climate in the Arctic should be considered by the atmosphere-ocean-cryosphere interaction.

It has to be noted that the simulation of surface albedo due to the transport of dust particles was subject to large uncertainties. The concentrations of impurities in snow were estimated by empirical equations but not in-situ measurement data. As a result, the cumulative effect of impurities in reducing the surface albedo was not considered. Also, the evolution of dust microphysical properties was not accounted in the model simulation. The atmospheric aging processes, i.e., dust particles coated with various type of aerosols during the long-range transport, could further enhance the reduction of snow albedo. The dust particle refractive index is regarded as an important factor for dust absorption in snowpack (He, 2022). To reduce the uncertainties of snow albedo simulation, simultaneous in-situ measurements of particle composition and optical properties in both the air and snowpack are essentially needed in the future Arctic studies.

Data availability

The measurement data at Barrow and Alert are from the EBAS database (https://ebas.nilu.no/). Aerosol columnar data are from AERONET (https://aeronet.gsfc.nasa.gov/). Aerosol vertical profiles are from AD-Net (https://www-lidar.nies.go.jp/AD-Net). The MODIS Level-3 aerosol products are from NASA's Giovanni (https://giovanni. gsfc.nasa.gov/giovanni/). The NCEP/NCAR reanalysis data are from https://www.esrl.noaa.gov/psd/data/gridded/reanalysis/

Author contributions

KH designed this study. XZ analyzed data. All reviewed and wrote the paper.

Competing interests

The authors declare that they have no conflict of interest.

Acknowledgements

We sincerely thank for EBAS, AERONET, AD-Net, NASA, and NCEP/NCAR for providing the observational and modeling data. This work was supported by the National Natural Science Foundation of China (42175119, 91644105) and the National Natural Science Foundation of Shanghai (18230722600). Kan Huang also acknowledges Jiangsu Shuangchuang Program through Jiangsu Fuyu Environmental Technology Co., Ltd.

References:

Blanchet, J. P. and List, R.: Estimation of optical properties of arctic haze using a numerical model, Atmosphere-Ocean, 21, 444-465, 10.1080/07055900.1983.9649179, 2010.

Breider, T. J., Mickley, L. J., Jacob, D. J., Ge, C., Wang, J., Sulprizio, M. P., Croft, B., Ridley, D. A., McConnell, J. R., Sharma, S., Husain, L., Dutkiewicz, V. A., Eleftheriadis, K., Skov, H., and Hopke, P. K.: Multidecadal trends in aerosol radiative forcing over the Arctic: Contribution of changes in anthropogenic aerosol to Arctic warming since 1980, Journal of Geophysical Research-Atmospheres, 122, 3573-3594, 10.1002/2016jd025321, 2017.

Brock, C. A., Cozic, J., Bahreini, R., Froyd, K. D., Middlebrook, A. M., McComiskey, A., Brioude, J., Cooper, O. R., Stohl, A., Aikin, K. C., de Gouw, J. A., Fahey, D. W., Ferrare, R. A., Gao, R. S., Gore, W., Holloway, J. S., Huebler, G., Jefferson, A., Lack, D. A., Lance, S., Moore, R. H., Murphy, D. M., Nenes, A., Novelli, P. C., Nowak, J. B., Ogren, J. A., Peischl, J., Pierce, R. B., Pilewskie, P., Quinn, P. K., Ryerson, T. B., Schmidt, K. S., Schwarz, J. P., Sodemann, H., Spackman, J. R., Stark, H., Thomson, D. S., Thornberry, T., Veres, P., Watts, L. A., Warneke, C., and Wollny, A. G.: Characteristics, sources, and transport of aerosols measured in spring 2008 during the aerosol, radiation, and cloud processes affecting Arctic Climate (ARCPAC) Project, Atmospheric Chemistry and Physics, 11, 2423-2453, 10.5194/acp-11-2423-2011, 2011.

CMA: (China Meteorological Administration Eds.): Sand-dust Weather Almanac (2011), China Meteorological Press, Beijing, China, 2013.

CMA: (China Meteorological Administration Eds.): Sand-dust Weather Almanac (2012), China Meteorological Press, Beijing, China, 2014.

CMA: (China Meteorological Administration Eds.): Sand-dust Weather Almanac (2013), China Meteorological Press, Beijing, China, 2015.

CMA: (China Meteorological Administration Eds.): Sand-dust Weather Almanac (2014), China Meteorological Press, Beijing, China, 2016.

CMA: (China Meteorological Administration Eds.): Sand-dust Weather Almanac (2015), China Meteorological Press, Beijing, China, 2017.

Dagsson-Waldhauserova, P., Renard, J. B., Olafsson, H., Vignelles, D., Berthet, G., Verdier, N., and Duverger, V.: Vertical distribution of aerosols in dust storms during the Arctic winter, Sci Rep-Uk, 9, 2019.

Di Biagio, C., Pelon, J., Ancellet, G., Bazureau, A., and Mariage, V.: Sources, Load, Vertical Distribution, and Fate of Wintertime Aerosols North of Svalbard From Combined V4 CALIOP Data, Ground-Based IAOOS Lidar Observations and Trajectory Analysis, Journal of Geophysical Research-Atmospheres, 123, 1363-1383, 10.1002/2017jd027530, 2018.

Di Pierro, M., Jaegle, L., and Anderson, T. L.: Satellite observations of aerosol transport from East Asia to the Arctic: three case studies, Atmospheric Chemistry and Physics, 11, 2225-2243, 10.5194/acp-11-2225-2011, 2011.

Domine, F., Cabanes, A., and Legagneux, L.: Structure, microphysics, and surface area of the Arctic snowpack near Alert during the ALERT 2000 campaign, Atmospheric Environment, 36, 2753-2765, 10.1016/s1352-2310(02)00108-5, 2002.

Dong, X., Xi, B., Crosby, K., Long, C. N., Stone, R. S., and Shupe, M. D.: A 10 year climatology of Arctic cloud fraction and radiative forcing at Barrow, Alaska, Journal of Geophysical Research-Atmospheres, 115, 10.1029/2009jd013489, 2010.

Dou, T., Xiao, C., Du, Z., Schauer, J. J., Ren, H., Ge, B., Xie, A., Tan, J., Fu, P., and Zhang, Y.: Sources, evolution and impacts of EC and OC in snow on sea ice: a measurement study in Barrow, Alaska, Science Bulletin, 62, 1547-1554, 10.1016/j.scib.2017.10.014, 2017.

Draxier, R. R. and Hess, G. D.: An overview of the HYSPLIT_4 modelling system for trajectories, dispersion and deposition, Aust Meteorol Mag, 47, 295-308, 1998.

Fan, S. M.: Modeling of observed mineral dust aerosols in the arctic and the impact on winter season low-level clouds, J Geophys Res-Atmos, 118, 11161-11174, 2013.

Ferrero, L., Ritter, C., Cappelletti, D., Moroni, B., Mocnik, G., Mazzola, M., Lupi, A., Becagli, S., Traversi, R., Cataldi, M., Neuber, R., Vitale, V., and Bolzacchini, E.: Aerosol optical properties in the Arctic: The role of aerosol chemistry and dust composition in a closure experiment between Lidar and tethered balloon vertical profiles, Sci Total Environ, 686, 452-467, 2019.

Fisher, J. A., Jacob, D. J., Wang, Q., Bahreini, R., Carouge, C. C., Cubison, M. J., Dibb, J. E., Diehl, T., Jimenez, J. L., Leibensperger, E. M., Lu, Z., Meinders, M. B. J., Pye, H. O. T., Quinn, P. K., Sharma, S., Streets, D. G., van Donkelaar, A., and Yantosca, R. M.: Sources, distribution, and acidity of sulfate-ammonium aerosol in the Arctic in winter-spring, Atmospheric Environment, 45, 7301-7318, 10.1016/j.atmosenv.2011.08.030, 2011.

Flanner, M. G.: Arctic climate sensitivity to local black carbon, Journal of Geophysical Research-Atmospheres, 118, 1840-1851, 10.1002/jgrd.50176, 2013.

Flanner, M. G., Zender, C. S., Randerson, J. T., and Rasch, P. J.: Present-day climate forcing and response from black carbon in snow, Journal of Geophysical Research-Atmospheres, 112, 10.1029/2006jd008003, 2007.

Gagne, M.-E., Fyfe, J. C., Gillett, N. P., Polyakov, I. V., and Flato, G. M.: Aerosol-driven increase in

Arctic sea ice over the middle of the twentieth century, Geophysical Research Letters, 44, 7338-7346, 10.1002/2016gl071941, 2017.

Gillett, N. P., Stone, D. A., Stott, P. A., Nozawa, T., Karpechko, A. Y., Hegerl, G. C., Wehner, M. F., and Jones, P. D.: Attribution of polar warming to human influence, Nature Geoscience, 1, 750-754, 10.1038/ngeo338, 2008.

Ginoux, P., Prospero, J. M., Gill, T. E., Hsu, N. C., and Zhao, M.: Global-Scale Attribution of Anthropogenic and Natural Dust Sources and Their Emission Rates Based on Modis Deep Blue Aerosol Products, Rev Geophys, 50, 2012.

Guo, J., Rahn, K. A., and Zhuang, G. S.: A mechanism for the increase of pollution elements in dust storms in Beijing, Atmos. Environ., 38, 855–862, 2004.

Guo, J., Lou, M., Miao, Y., Wang, Y., Zeng, Z., Liu, H., He, J., Xu, H., Wang, F., Min, M., and Zhai, P.: Trans-Pacific transport of dust aerosols from East Asia: Insights gained from multiple observations and modeling, Environmental Pollution, 230, 1030-1039, 10.1016/j.envpol.2017.07.062, 2017.

Hansen, J. and Nazarenko, L.: Soot climate forcing via snow and ice albedos, Proceedings of the National Academy of Sciences of the United States of America, 101, 423-428, 10.1073/pnas.2237157100, 2004.

He, C.: Modelling light-absorbing particle–snow–radiation interactions and impacts on snow albedo: fundamentals, recent advances and future directions, Environmental Chemistry, 10.1071/EN22013, 2022.

Holben, B. N., Eck, T. F., Slutsker, I., Tanre, D., Buis, J. P., Setzer, A., Vermote, E., Reagan, J. A., Kaufman, Y. J., Nakajima, T., Lavenu, F., Jankowiak, I., and Smirnov, A.: AERONET - A federated instrument network and data archive for aerosol characterization, Remote Sens Environ, 66, 1-16, Doi 10.1016/S0034-4257(98)00031-5, 1998.

Hsu, N. C., M.-J. Jeong, C. Bettenhausen, A. M. Sayer, R. Hansell, C. S. Seftor, J. Huang, and S.-C. Tsay (2013), Enhanced Deep Blue aerosol retrieval algorithm: The second generation, J. Geophys. Res. Atmos.,118, 9296–9315,doi:10.1002/jgrd.50712.Huang, Z., Huang, J., Hayasaka, T., Wang, S., Zhou, T., and Jin, H.: Short-cut transport path for Asian dust directly to the Arctic: a case study, Environmental Research Letters, 10, 10.1088/1748-9326/10/11/114018, 2015a.

Huang, Z. W., Huang, J. P., Hayasaka, T., Wang, S. S., Zhou, T., and Jin, H. C.: Short-cut transport path for Asian dust directly to the Arctic: a case study, Environ Res Lett, 10, 2015b.

Kaspari, S., Painter, T. H., Gysel, M., Skiles, S. M., and Schwikowski, M.: Seasonal and elevational variations of black carbon and dust in snow and ice in the Solu-Khumbu, Nepal and estimated radiative forcings, Atmospheric Chemistry and Physics, 14, 8089-8103, 10.5194/acp-14-8089-2014, 2014.

Koch, D. and Del Genio, A. D.: Black carbon semi-direct effects on cloud cover: review and synthesis, Atmospheric Chemistry and Physics, 10, 7685-7696, 10.5194/acp-10-7685-2010, 2010.

Kylling, A., Zwaaftink, C. D. G., and Stohl, A.: Mineral Dust Instantaneous Radiative Forcing in the Arctic, Geophys Res Lett, 45, 4290-4298, 2018.

Levy, R. C., L. A. Remer, S. Mattoo, E. F. Vermote, and Y. J. Kaufman (2007), Second-generation operational algorithm: Retrieval of aerosol properties over land from inversion of Moderate Resolution Imaging Spectroradiometer spectral reflectance, J. Geophys. Res.,112, D13211, doi:10.1029/2006JD007811.

Liu, D., Qi, F. D., Jin, C. J., Yue, G. M., and ZHou, J.: Polarization lidar observations of cirrus clouds and Asian dust aerosols over Hefei, Chinese Journal of Atmospheric Sciences, 27, 1093 - 1100, 2003.

Liu, H., Liu, X. D., and Dong, B. W.: Influence of Central Siberian Snow-Albedo Feedback on the Spring East Asian Dust Cycle and Connection With the Preceding Winter Arctic Oscillation, J Geophys Res-Atmos, 123, 13368-13385, 2018.

Marelle, L., Raut, J. C., Thomas, J. L., Law, K. S., Quennehen, B., Ancellet, G., Pelon, J., Schwarzenboeck, A., and Fast, J. D.: Transport of anthropogenic and biomass burning aerosols from Europe to the Arctic during spring 2008, Atmospheric Chemistry and Physics, 15, 3831-3850, 10.5194/acp-15-3831-2015, 2015.

Mishra, M. K., Rajeev, K., Thampi, B. V., Parameswaran, K., and Nair, A. K. M.: Micro pulse lidar observations of mineral dust layer in the lower troposphere over the southwest coast of Peninsular India during the Asian summer monsoon season, Journal of Atmospheric and Solar-Terrestrial Physics, 72, 1251-1259, 10.1016/j.jastp.2010.08.012, 2010.

Omar, A. H., et al. (2009), The CALIPSO automated aerosol classification and lidar ratio selection algorithm, J. Atmos. Oceanic Technol.,26,1994–2014, doi:10.1175/2009JTECHA1231.1.Pitchford, M., Malm, W., Schichtel, B., Kumar, N., Lowenthal, D., and Hand, J.: Revised algorithm for estimating light extinction from IMPROVE particle speciation data, J Air Waste Manage, 57, 1326-1336, 10.3155/1047-3289.57.11.1326, 2007.

Qi, L., Li, Q., Henze, D. K., Tseng, H.-L., and He, C.: Sources of springtime surface black carbon in the Arctic: an adjoint analysis for April 2008, Atmospheric Chemistry and Physics, 17, 9697-9716, 10.5194/acp-17-9697-2017, 2017.

Quinn, P. K., Bates, T. S., Baum, E., Doubleday, N., Fiore, A. M., Flanner, M., Fridlind, A., Garrett, T. J., Koch, D., Menon, S., Shindell, D., Stohl, A., and Warren, S. G.: Short-lived pollutants in the Arctic: their climate impact and possible mitigation strategies, Atmospheric Chemistry and Physics, 8, 1723-1735, 10.5194/acp-8-1723-2008, 2008.

Ranjbar, K., O'Neill, N. T., Ivanescu, L., King, J., and Hayes, P. L.: Remote sensing of a high-Arctic, local dust event over Lake Hazen (Ellesmere Island, Nunavut, Canada), Atmos Environ, 246, 2021.

Sand, M., Berntsen, T. K., Seland, O., and Kristjansson, J. E.: Arctic surface temperature change to emissions of black carbon within Arctic or midlatitudes, Journal of Geophysical Research-Atmospheres, 118, 7788-7798, 10.1002/jgrd.50613, 2013a.

Sand, M., Berntsen, T. K., Kay, J. E., Lamarque, J. F., Seland, O., and Kirkevag, A.: The Arctic response to remote and local forcing of black carbon, Atmospheric Chemistry and Physics, 13, 211-224, 10.5194/acp-13-211-2013, 2013b.

Screen, J. A. and Simmonds, I.: The central role of diminishing sea ice in recent Arctic temperature amplification, Nature, 464, 1334-1337, 10.1038/nature09051, 2010.

Serreze, M. C. and Francis, J. A.: The arctic amplification debate, Climatic Change, 76, 241-264, 10.1007/s10584-005-9017-y, 2006.

Serreze, M. C., Barrett, A. P., Stroeve, J. C., Kindig, D. N., and Holland, M. M.: The emergence of surface-based Arctic amplification, Cryosphere, 3, 11-19, 10.5194/tc-3-11-2009, 2009.

Sharma, S., Ishizawa, M., Chan, D., Lavoue, D., Andrews, E., Eleftheriadis, K., and Maksyutov, S.: 16-year simulation of Arctic black carbon: Transport, source contribution, and sensitivity analysis on deposition, Journal of Geophysical Research-Atmospheres, 118, 943-964, 10.1029/2012jd017774, 2013.

Shimizu, A., Nishizawa, T., Jin, Y., Kim, S. W., Wang, Z. F., Batdorj, D., and Sugimoto, N.: Evolution of a lidar network for tropospheric aerosol detection in East Asia, Opt Eng, 56, 2017.

Shindell, D. and Faluvegi, G.: Climate response to regional radiative forcing during the twentieth century, Nature Geoscience, 2, 294-300, 10.1038/ngeo473, 2009.

Sobhani, N., Kulkarni, S., and Carmichael, G. R.: Source sector and region contributions to black carbon and PM2.5 in the Arctic, Atmospheric Chemistry and Physics, 18, 18123-18148, 10.5194/acp-18-18123-2018, 2018.

Stohl, A.: Characteristics of atmospheric transport into the Arctic troposphere, Journal of Geophysical Research-Atmospheres, 111, 10.1029/2005jd006888, 2006.

Stone, R. S., Dutton, E. G., Harris, J. M., and Longenecker, D.: Earlier spring snowmelt in northern Alaska as an indicator of climate change, Journal of Geophysical Research-Atmospheres, 107, 10.1029/2000jd000286, 2002.

Wang, Q., Dong, X., Fu, J. S., Xu, J., Deng, C., Jiang, Y., Fu, Q., Lin, Y., Huang, K., and Zhuang, G.: Environmentally dependent dust chemistry of a super Asian dust storm in March 2010: observation and simulation, Atmos Chem Phys, 2018a.

Wang, Z., Pan, X., Uno, I., Chen, X., Yamamoto, S., Zheng, H., Li, J., and Wang, Z.: Importance of mineral dust and anthropogenic pollutants mixing during a long-lasting high PM event over East Asia, Environmental Pollution, 234, 368-378, 10.1016/j.envpol.2017.11.068, 2018b.

Warneke, C., Froyd, K. D., Brioude, J., Bahreini, R., Brock, C. A., Cozic, J., de Gouw, J. A., Fahey, D. W., Ferrare, R., Holloway, J. S., Middlebrook, A. M., Miller, L., Montzka, S., Schwarz, J. P., Sodemann, H., Spackman, J. R., and Stohl, A.: An important contribution to springtime Arctic aerosol from biomass burning in Russia, Geophysical Research Letters, 37, 10.1029/2009gl041816, 2010.

Weijers, S., Buchwal, A., Blok, D., Loeffler, J., and Elberling, B.: High Arctic summer warming tracked by increased Cassiope tetragona growth in the world's northernmost polar desert, Global Change Biology, 23, 5006-5020, 10.1111/gcb.13747, 2017.

Xu, L., Fukushima, S., Sobanska, S., Murata, K., Naganuma, A., Liu, L., Wang, Y., Niu, H., Shi, Z., Kojima, T., Zhang, D., and Li, W.: Tracing the evolution of morphology and mixing state of soot particles along with the movement of an Asian dust storm, *Atmos. Chem. Phys*., 20, 14321-14332, 10.5194/acp-20-14321-2020, 2020.

Zhang, Y. L., Kang, S. C., Cong, Z. Y., Schmale, J., Sprenger, M., Li, C. L., Yang, W., Gao, T. G., Sillanpaa, M., Li, X. F., Liu, Y. J., Chen, P. F., and Zhang, X. L.: Light-absorbing impurities enhance glacier albedo reduction in the southeastern Tibetan plateau, J Geophys Res-Atmos, 122, 6915-6933, 10.1002/2016jd026397, 2017.

Zwaaftink, C. D. G., Grythe, H., Skov, H., and Stohl, A.: Substantial contribution of northern high-latitude sources to mineral dust in the Arctic, Journal of Geophysical Research-Atmospheres, 121, 13678-13697, 10.1002/2016jd025482, 2016.